Computers and Mathematics with Applications 78 (2019) 707–722

Contents lists available at ScienceDirect

Computers and Mathematics with Applications

journal homepage: www.elsevier.com/locate/camwa

Prediction of evanescent coupling efficiency in two parallel silica nanowires

Tony W.H. Sheu [a,b,c,*], C.Y. Kao [a], Y.W. Chang [a], J.H. Li [a]

[a] Department of Engineering Science and Ocean Engineering, National Taiwan University, No. 1, Sec. 4, Roosevelt Road, Taipei, Taiwan, Republic of China
[b] Center for Advanced Study in Theoretical Sciences (CASTS), National Taiwan University, Taipei, Taiwan
[c] Institute of Applied Mathematical Sciences, National Taiwan University, Taipei, Taiwan

ARTICLE INFO

Article history:
Received 10 April 2018
Received in revised form 28 November 2018
Accepted 21 February 2019
Available online 9 March 2019

Keywords:
Maxwell's equations
Evanescent wave
Silica nanowires
Coupling efficiency
Symplectic partitioned Runge–Kutta
Phase velocities

ABSTRACT

In this study the efficiency of evanescent wave coupling between two air-clad silica nanowires in single-mode operation is numerically predicted in time-domain using the finite difference method. To this end, a three-dimensional scheme developed for solving the Maxwell's equations on staggered grids will be employed. The electric and magnetic field solutions are sought subjected to the zero-divergence condition (or Gauss's law) in discrete level. In addition, we aim to conserve Hamiltonians existing in ideal Maxwell's equations at all times by adopting the explicit second-order accurate symplectic partitioned Runge–Kutta temporal scheme. Moreover, all the spatial derivative terms in the Faraday's and Ampère's equations are approximated by the proposed scheme which can render not only fourth-order spatial accuracy, but also minimize the discrepancy between the exact and the derived numerical phase velocities.

1. Introduction

In areas of optical communication, power delivery, and sensing, silica (SiO_2) waveguides with diameters greater than the wavelength of transmitted light have been widely applied in the past three to four decades. With the rapid progress in fabrication technique, low-loss air-clad waveguides with subwavelength diameters desirable for photonic device applications are now practically available. An increasing demand on the designs of these modern waveguides for industrial applications has attracted intensive research recently. In this study, subwavelength-diameter silica nanowires, which have been known to be one of the promising building blocks for couplers, modulators, resonators, lasers and sensors, are considered. We aim to predict the efficiency of evanescent wave coupling in two parallel nanowires.

Subjected to an incident electromagnetic wave, schematically shown in Fig. 1, with the wavelength of 633 nm, its energy shall be concentrated along the direction of wire (or horizontal direction). The field strength decreases sharply in an exponential-like manner in the direction away from the wire surface, leaving it concentrated only in a region fairly close to the interface. This type of surface wave propagating along the waveguide surface has been referred to as the evanescent wave.

Evanescent waves have many applications in optics and acoustics. One can exploit electromagnetic evanescent waves to exert optical radiation pressure on small particles to achieve different design goals. One can refer to [1] for other

* Corresponding author at: Department of Engineering Science and Ocean Engineering, National Taiwan University, No. 1, Sec. 4, Roosevelt Road, Taipei, Taiwan, Republic of China.
E-mail address: twhsheu@ntu.edu.tw (T.W.H. Sheu).

https://doi.org/10.1016/j.camwa.2019.02.033
0898-1221/

applications in the presence of an evanescent wave. In this study, we are interested to understand more about the evanescent wave coupling mechanism between two parallel optical nanowires which allow a single-mode operation and have a low optical loss.

We consider evanescent wave propagation in parallelly configured silica nanowires whose diameters are very small. The parameters such as permittivity (ϵ) and permeability (μ) can be used to describe the response of a dielectric silica to an incident electromagnetic field. The ideal Maxwell's equations, as a result, can be reasonably applied to model wave propagation in silica because of its constant dielectric property in visible light region. The finite difference method developed in time-domain has advantage in conducting wave simulation due to its simplicity in programming and in computer storage capacity [2,3]. Therefore, the Finite Difference Time Domain (FDTD) method is employed in the present study to approximate Maxwell's equations on staggered grids. Our objective is to compute the divergence-free electromagnetic field solutions.

While approximating the derivative terms in Maxwell's equations, the numerically introduced dissipation error can smear wave solution profile. Moreover, the dispersion error can lead to an inaccurately predicted phase speed or group velocity [4,5]. Since numerically introduced dispersion error can make the scheme less stable, it is essential to develop a dispersion-error reducing method and apply it to approximate the first-order spatial derivative terms. Prediction of correct propagation characteristics is the second objective of our scheme development for solving the Maxwell's equations. On the long time simulation of the electromagnetic wave prediction, the solution quality can be seriously deteriorated by the other kind of numerical error arising from the application of non-symplectic temporal schemes. Preserving the symplectic property in long-term simulation of Maxwell's equations motivated us to properly approximate the time derivative terms shown in the Faraday's and Ampère's equations.

The rest of this paper is organized as follows. In Section 2, the Maxwell's equations for simulating EM wave propagation in non-dispersive silica nanowires are presented. Some remarkable features of the Maxwell's equations, which are essential to develop a better numerical scheme in time-domain, are briefly described. In Section 3, the lossless Maxwell's equations are approximated in space and time underlying their respective mathematical theories. The explicit symplectic PRK (Partitioned Runge–Kutta) temporal scheme developed to conserve Hamiltonians in the ideal Maxwell's equations is applied. Based on the employed explicit scheme, its corresponding numerical dispersion relation equation (DRE) can be derived. The scheme endowed with the optimized numerical phase velocity feature is also verified in Section 3. Then, we will describe the evanescent wave problem in Section 4 and discuss the results predicted in the investigated parallel silica nanowires in Section 5 aiming to gain a better understanding of the coupling efficiency between two parallel nanowires. Finally, some concluding remarks are drawn in Section 6.

2. Mathematical model

In visible light region, the dielectric constant of silica remains almost unchanged. As a result, a set of Maxwell's equations including three Faraday's equations, three Ampère's equations and two Gauss's equations for modelling non-dispersive silica in visible light region is employed for solving the field variables $\underline{E} = \left(E_x, E_y, E_z\right)^T$ and $\underline{H} = \left(H_x, H_y, H_z\right)^T$

$$\frac{\partial \underline{H}}{\partial t} = -\frac{1}{\mu} \nabla \times \underline{E}, \tag{1}$$

$$\frac{\partial \underline{E}}{\partial t} = \frac{1}{\epsilon} \nabla \times \underline{H}. \tag{2}$$

The above Maxwell's equations defined in vacuum are known to have many mathematically intriguing properties which all play key roles in determining the quality of the finite difference solution predicted in time-domain. The helicity Hamiltonian H_1 of the currently investigated infinite-dimensional Hamiltonian equations (1)–(2) is given below [6]

$$H_1 = \frac{1}{2} \int \frac{1}{\epsilon} \underline{H} \cdot \nabla \times \underline{H} + \frac{1}{\mu} \underline{E} \cdot \nabla \times \underline{E} \, d\Omega. \tag{3}$$

The other quadratic Hamiltonian (or energy density) is given below [7]

$$H_2 = \frac{1}{2} \int \mu \underline{H} \cdot \underline{H} + \epsilon \underline{E} \cdot \underline{E} \, d\Omega. \tag{4}$$

Both Hamiltonians H_1 and H_2 will be considered in our discussion of three-dimensional simulated results.

In the presence of eight differential equations, two of Maxwell's equations shall be neglected for uniquely computing a total number of six solutions for $\underline{E}$ and $\underline{H}$. Note that Gauss's law is normally not taken into account since the divergence-free equations for $\underline{H}$ and $\underline{E}$ can be derived analytically from the Faraday's law and Ampère's law, respectively, within the continuous context. However, calculation of the EM wave solutions from Faraday's and Ampère's equations may cause the computed magnetic and electric fields no longer to satisfy two divergence free conditions. One can circumvent this simulation problem by discretizing the Maxwell equations on staggered grids. The other way of overcoming this computational difficulty is to force the magnetic and electric divergences towards zero by adding, for example, two properly introduced gradient terms into the Maxwell's equations [8–10].

3. Numerical model

Faraday's and Ampère's equations (1)–(2) constitute a Hamiltonian differential system. It is therefore necessary to numerically preserve the symplectic structure and conserve the total energy. To this end, the second-order accurate explicit symplectic partitioned Runge–Kutta scheme presented in [11] is adopted to approximate the time derivative terms shown in (1)–(2).

When applying the finite difference method to solve the hyperbolic Maxwell's equations in time-domain, we need to reduce the dispersion and anisotropy errors [12,13]. To this end, all the spatial derivative terms shown in their resulting semi-discretized equations will be approximated using the modified equation analysis and the dispersion analysis detailed in [14].

On staggered grids, the first-order derivative terms $\frac{\partial H_y^n}{\partial x}$ and $\frac{\partial H_x^n}{\partial y}$ at the interior node $(i, j, k+\frac{1}{2})$ are approximated as

$$\frac{\partial H_y}{\partial x}\Big|_{i,j,k+\frac{1}{2}}^n = \frac{1}{h}\left[a_1\left(H_y|_{i+\frac{5}{2},j,k+\frac{1}{2}}^n - H_y|_{i-\frac{5}{2},j,k+\frac{1}{2}}^n\right) + a_2\left(H_y|_{i+\frac{3}{2},j,k+\frac{1}{2}}^n - H_y|_{i-\frac{3}{2},j,k+\frac{1}{2}}^n\right) + a_3\left(H_y|_{i+\frac{1}{2},j,k+\frac{1}{2}}^n - H_y|_{i-\frac{1}{2},j,k+\frac{1}{2}}^n\right)\right], \tag{5}$$

$$\frac{\partial H_x}{\partial y}\Big|_{i,j,k+\frac{1}{2}}^n = \frac{1}{h}\left[a_1\left(H_x|_{i,j+\frac{5}{2},k+\frac{1}{2}}^n - H_x|_{i,j-\frac{5}{2},k+\frac{1}{2}}^n\right) + a_2\left(H_x|_{i,j+\frac{3}{2},k+\frac{1}{2}}^n - H_y|_{i,j-\frac{3}{2},k+\frac{1}{2}}^n\right) + a_3\left(H_x|_{i,j+\frac{1}{2},k+\frac{1}{2}}^n - H_x|_{i,j-\frac{1}{2},k+\frac{1}{2}}^n\right)\right]. \tag{6}$$

The coefficients a_1, a_2 and a_3 will be determined theoretically below.

It is worthy to note that we intend to reduce the numerical dispersion error in order to get accurately predicted propagation characteristics in Maxwell's equations. The strategy of achieving this goal is to equate the numerical phase velocity and the exact phase velocity $\underline{\upsilon}_p\ (\equiv \frac{\omega_{num}}{\underline{k}})$ in the integral range of $-m_p\pi \le h\underline{k} \le m_p\pi$. As a result, the error function defined as $\left[|\frac{\omega_{num}}{\underline{k}}| - |\frac{\omega_{exact}}{\underline{k}}|\right]^2$ is minimized in the following weak sense

$$E_p = \int_{-m_p\pi}^{m_p\pi}\left[|\frac{\omega_{num}}{\underline{k}}| - |\frac{\omega_{exact}}{\underline{k}}(\equiv c)|\right]^2 W_p\ d(k_x\Delta x)\ d(k_y\Delta y)\ d(k_z\Delta z). \tag{7}$$

In the above, $k_x\Delta x$, $k_y\Delta y$ and $k_z\Delta z$ denote the scaled (or modified) wavenumbers along x, y and z directions, respectively. The function W_p introduced into the above error minimization procedure is for analytically integrating Eq. (7). The value of $m_p\ (=\frac{1}{2})$ has been chosen mainly for reducing much of the aliasing error [14]. It is noted that the exact and numerical dispersion relation equations have been derived in detail in (8) and (9)

$$\left(\frac{\omega_{exact}}{c}\right)^2 = k_x^2 + k_y^2 + k_z^2. \tag{8}$$

$$\begin{aligned}\frac{1}{c^2}\frac{\omega_{num}^2}{4}\left(\frac{sin(\omega_{num}\Delta t/2)}{\omega_{num}\Delta t}\right)^2 = {} & k_x^2\left(\frac{5}{2}a_1\frac{sin(\frac{5}{2}k_x\Delta x)}{\frac{5}{2}k_x\Delta x} + \frac{3}{2}a_2\frac{sin(\frac{3}{2}k_x\Delta x)}{\frac{3}{2}k_x\Delta x} + \frac{1}{2}a_3\frac{sin(\frac{1}{2}k_x\Delta x)}{\frac{1}{2}k_x\Delta x}\right)^2 \\ & + k_y^2\left(\frac{5}{2}a_1\frac{sin(\frac{5}{2}k_y\Delta y)}{\frac{5}{2}k_y\Delta y} + \frac{3}{2}a_2\frac{sin(\frac{3}{2}k_y\Delta y)}{\frac{3}{2}k_y\Delta y} + \frac{1}{2}a_3\frac{sin(\frac{1}{2}k_y\Delta y)}{\frac{1}{2}k_y\Delta y}\right)^2 \\ & + k_z^2\left(\frac{5}{2}a_1\frac{sin(\frac{5}{2}k_z\Delta z)}{\frac{5}{2}k_z\Delta z} + \frac{3}{2}a_2\frac{sin(\frac{3}{2}k_z\Delta z)}{\frac{3}{2}k_z\Delta z} + \frac{1}{2}a_3\frac{sin(\frac{1}{2}k_z\Delta z)}{\frac{1}{2}k_z\Delta z}\right)^2.\end{aligned} \tag{9}$$

The minimal value of E_p in (7) is obtained at the limiting condition $\frac{\partial E_p}{\partial a_3} = 0$. This procedure of minimization yields one algebraic equation

$$\begin{aligned}& + 0.013462\ a_3^2a_1 + 0.024686\ a_2^3 - 0.003317\ a_2 - 0.004562\ a_1 + 0.075261\ a_1a_2a_3 \\ & + 0.105823\ a_1a_2^2 + 0.078272\ a_1^3 + 0.001195\ a_3^3 + 0.155929\ a_1^2a_2 + 0.054814\ a_1^2a_3 \\ & + 0.026761\ a_3a_2^2 + 0.009749\ a_3^2a_2 - 0.001222\ a_3 = 0\end{aligned} \tag{10}$$

Eq. (10) is then applied together with the other two algebraic equations given below, which are (11) and (12) derived from the modified equation analysis of second kind.

$$5a_1 + 3a_2 + a_3 = 1, \tag{11}$$

and

$$\frac{125}{24}a_1 + \frac{9}{8}a_2 + \frac{1}{24}a_3 - \frac{Cr^2}{24}(5a_1 + 3a_2 + a_3) = 0. \tag{12}$$

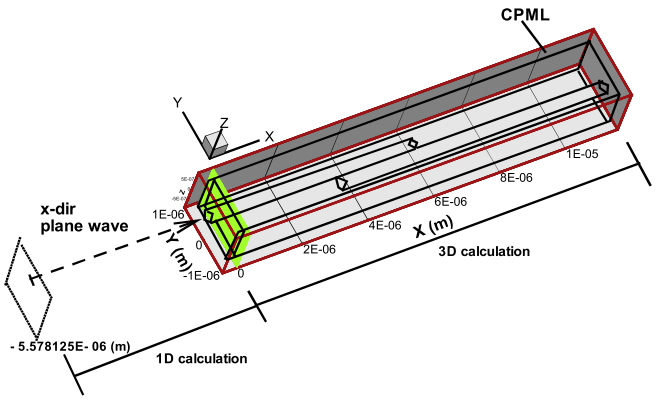

Fig. 1. Schematic of the investigated two overlapped parallel nanowires.

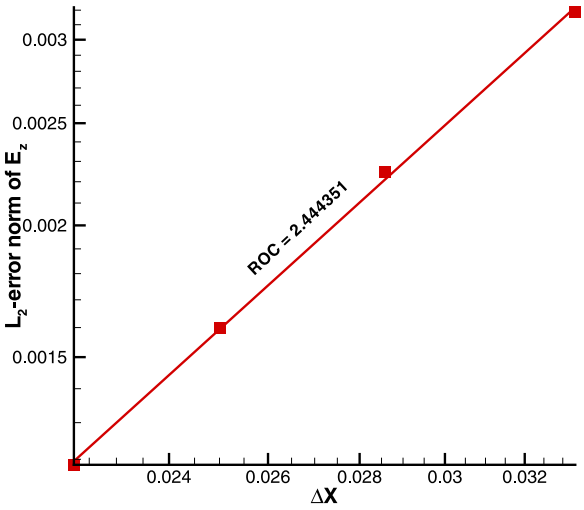

Fig. 2. The computed L_2 error norms are plotted with respect to grid spacings to get the spatial rate of convergence.

The three introduced coefficients can then be obtained as $a_1 = -0.0002985$, $a_2 = -0.0385073$ and $a_3 = 1.1170147$. By virtue of the above minimization procedure implemented in wavenumber space and the modified equation analysis for $\frac{\partial H_x}{\partial x}$, the proposed space-centred scheme has fourth-order spatial accuracy because the derived modified equation is $\frac{\partial H_x}{\partial x} = \frac{\partial H_x}{\partial x}|_{exact} - 0.00489575\, h^4 \frac{\partial^5 H_x}{\partial x^5} + O(h^6) + \cdots$.

For the verification of the applied explicit symplectic PRK temporal scheme and the spatial scheme capable of preserving dispersion relation equation on staggered grids, the Maxwell's equations in $-1 \le x \le 1$, $-1 \le y \le 1$ and $-1 \le z \le 1$ are amenable to the analytic solutions given in [15] investigated at $\mu = 1$ and $\epsilon = 1$

$$E_x = \cos(2\pi(x+y+z) - 2\sqrt{3}\pi t), \quad E_y = -2E_x,$$
$$E_z = E_x, \quad H_x = \sqrt{3}E_x, \quad H_y = 0, \quad H_z = -\sqrt{3}E_x. \tag{13}$$

Subject to the initial conditions by setting $t = 0$ in Eq. (13), the computed errors are tabulated in Table 1 and the corresponding spatial rate of convergence is plotted in Fig. 2. The proposed dual-preserving scheme in free space for the TM-mode Maxwell's equations is verified. The resulting deviation between the predicted spatial rate of convergence 2.44435 and the theoretical order of accuracy (i.e. 4) is mainly due to the use of one-sided second-order accurate scheme applied at the end points and at the points next to the end points (see Table 2).

The predicted and exact energy densities given in (4) are plotted against time in Fig. 3. Note that the Hamiltonian defined in (3) is equal to zero. The predicted value of $\nabla \cdot \underline{H}$ is almost equal to zero, as shown in Fig. 4, indicating that the Gauss's law is satisfied in the discrete level by using the employed explicit symplectic partitioned Runge–Kutta scheme.

Table 1
Comparison of the computed L_2- *error norms* at $t = 5$ (s) using the current and Yee's schemes.

Present			Yee [2]		
L_2-error norm	Grid	CPU time (s)	L_2-error norm	Grid	CPU time (s)
3.1852E−03	$61 \times 61 \times 61$	15.2725	3.2169E−03	$218 \times 218 \times 218$	1363.6359
2.2449E−03	$71 \times 71 \times 71$	28.6730	2.24778E−03	$260 \times 260 \times 260$	2731.1719
1.5974E−03	$81 \times 81 \times 81$	48.7659	1.6084E−03	$308 \times 308 \times 308$	5438.8657

Table 2
Comparison of the computed L_2- *error norms* and the *CPU* times based on the results computed at $t = 5$ (s).

	L_2-error norm		CPU time (seconds)	
	Present	Yee [2]	Present	Yee [2]
$41 \times 41 \times 41$	4.6573E−02	0.1107	1.1388	0.5772
$51 \times 51 \times 51$	2.1792E−02	0.1031	2.8548	1.3884
$61 \times 61 \times 61$	7.1823E−03	7.3707E−02	5.8032	3.0264
$71 \times 71 \times 71$	2.6276E−03	5.1761E−02	10.3273	5.2260

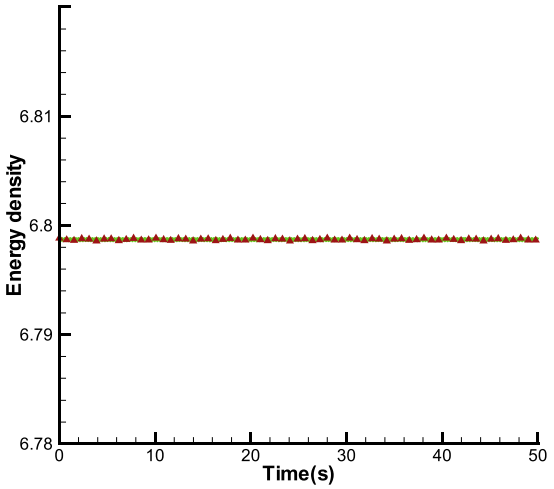

Fig. 3. The predicted and exact energy densities are plotted with respect to time.

4. Description of the evanescent wave problem

In the prediction of the coupling efficiency between two optical nanowires of short length, we can reasonably assume that the parallel wires under investigation are not dissipative and are source free. Under these assumptions, the Maxwell's equations can be reduced to a much simplified set of one-dimensional Helmholtz equations given below along the z-direction in the first wire between $x = -1.1375$ μm and $x = 0$ μm schematically shown in Fig. 1

$$(\nabla^2 + k^2 - \beta^2)E_z = 0,$$
$$(\nabla^2 + k^2 - \beta^2)H_z = 0, \tag{14}$$

where $k = 2\pi/\lambda = n^2 k_0^2$ and β is denoted as the propagation constant. Note that, $\nabla^2 = \frac{\partial^2}{\partial r^2} + \frac{1}{r}\frac{\partial}{\partial r} + \frac{1}{r^2}\frac{\partial^2}{\partial \phi^2}$ in cylindrical coordinates.

The exact solution for the z-dependence Helmholtz equation takes the form of $(E_z, H_z)^T = (E_z, H_z)^T(r)exp(\pm il\phi)$, where $l = 0, 1, 2, \ldots$. The equation for $\underline{\Psi} = (E_z, H_z)^T$ turns out to be the Bessel equation. The exact solution (or Bessel function of order l) of the even/odd mode can be derived inside and outside of the core of nanowires. The reader can refer to [16] or [17] for the derivation of exact solutions.

Having derived the exact solution which is the function of propagation constant β, we need to determine its value for the investigated subwavelength-diameter silica wire so as to get the incident wave solution. The wave under consideration involves a silica wire of diameter $2a = 350$ nm with $n_1 = 1.46$ operated in single mode with the wavelength $\lambda = 633$ nm. According to the equation derived below or the values of J_{l-1} and haJ_l plotted with respect to the value of ha in Fig. 5

$$\frac{J_{l-1}(ha)}{haJ_l(ha)} = -\left(\frac{n_1^2 + n_2^2}{2n_1^2}\right)\frac{K_l'(qa)}{qaK_l(qa)} + \left[\frac{1}{(ha)^2} - R\right], \tag{15}$$

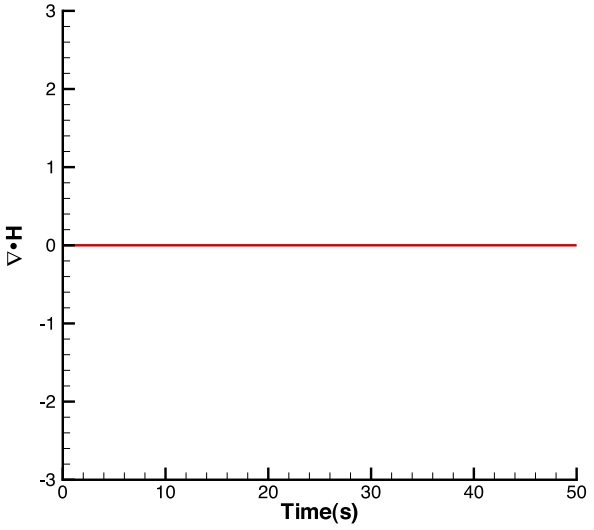

Fig. 4. The predicted value of $\nabla \cdot \underline{H}$ is plotted with respect to time.

we can get $ha = 1.6118125$ or $h = 9205714.286$. In the above, $R = [(\frac{n_1^2-n_2^2}{2n_1^2})^2(\frac{K_l'(qa)}{qaK_l(qa)})^2 + (\frac{l\beta}{n_1k_0})^2(\frac{1}{q^2a^2} + \frac{1}{h^2a^2})^2]^{1/2}$. Note that $h = (n_1^2k_0^2 - \beta^2)^{1/2}$, where $k_0 = 2\pi/\lambda = 9926043.139$. Now, for the nanowire of radius 175 nm operated in single frequency (or in wavelength of 633 nm), the propagation constant can be determined as $\beta = 11192566.94$. This value lies exactly on the β curve, which is plotted with respect to $2a$, shown in Fig. 6.

Following the above z-dependence exact solution derived in the wire between $x = -5.578125$ μm and $x = 0$ μm, simulation will be carried out in the domain schematically shown in Fig. 1. The solution is sought subjected to a time harmonic incident wave of amplitude 1. For clearness, the incident electric field $E_z(y, z)$ specified at the plane $x = 0$ μm is plotted in Fig. 7.

The nanowire system under investigation involves two cylindrical silica nanowires which have the same diameter $d = 350$ nm. These wires placed in parallel and separated by a width of $H = 0$ are overlapped by different lengths of L. The refractive index of the two silica nanowires under investigation is $n_1 = 1.46$, whereas the refractive index of air n_a is 1. The magnitude of the V-number, defined as $V = \frac{\pi d}{n\lambda}(n^2 - n_a^2)$, is chosen to be 2.405. The wavelength of the propagating light (or $\lambda = 633$ nm) inside the wire permits single-mode operation [18].

While simulating the EM wave equations (1)–(2) in an open domain, the physical domain needs to be truncated somewhere because of the limited availability of computer time and memory. In this simulation, we attempt to overcome this practical difficulty by prescribing a proper boundary condition at users' truncated boarder to prevent wave re-entry into the analysis domain and interact with the outgoing wave as time elapses. The Convolutional Perfectly Matched Layer (CPML) method [19] is applied to calculate the time-dependent solutions from the Maxwell's equations in the domain schematically shown in Fig. 1, which contains the absorbing layer.

5. Discussion of results

When two nanowires are in close proximity, they tend to attract each other through the electrostatic force. Under the circumstances, perturbation theory can no longer be suitably applied to study the mode efficiency of coupling, which is defined as the fraction of the available output from the upper nanowire (source). We must resort to numerical approach to calculate the evanescent coupling efficiency. In this study, we will keep the wire diameter unchanged but allow it to be varied with the overlapping length L. The resulting evanescent wave coupling in two nanowires will be investigated in detail in the following sections.

5.1. The effect of overlapping lengths on the coupling coefficient

Under the condition of the same nanowire diameter, the coupling efficiency of two parallel nanowires will be numerically calculated at different overlapping lengths. In this study, fifteen overlapping lengths, namely $L = 0$ μm, 0.30625 μm, 0.590625 μm, 0.896875 μm, 1.203125 μm, 1.793750 μm, 1.990625 μm, 2.40625 μm, 2.996875 μm, 3.303125 μm, 3.605 μm, 3.89375 μm, 4.06875 μm, 4.790625 μm, 5.096875 μm, are investigated at the condition of $a = 175$ nm. Based on the simulated 3D solutions using the proposed solver, we can first calculate their x-components of the Poynting vector and plot them, for example, at $t = 7.29 \times 10^{-5}$ s at different values of L. The computed time-dependent values of $P_x(x, t)$ are then integrated over a time period T to obtain the averaged value of $P_{x,ave}(x) \equiv \frac{1}{T}\int_0^T P_x(x, t)dt$. This

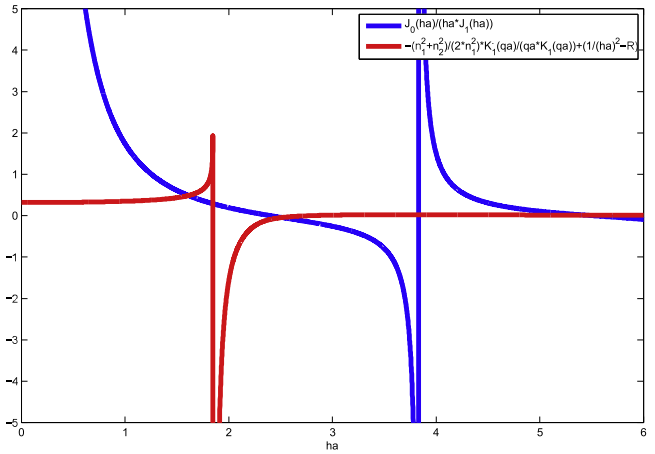

Fig. 5. The magnitudes of the terms on the left (blue) and right (red) sides of Eq. (15) are plotted against the value of *ha*.

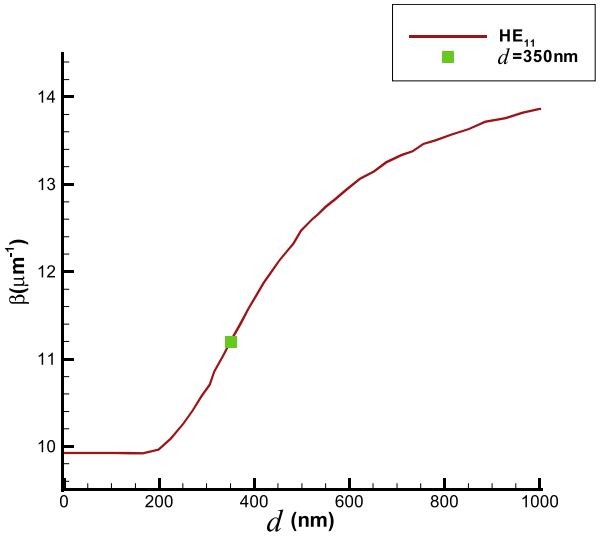

Fig. 6. The plot of the coefficient β with respect to *d*.

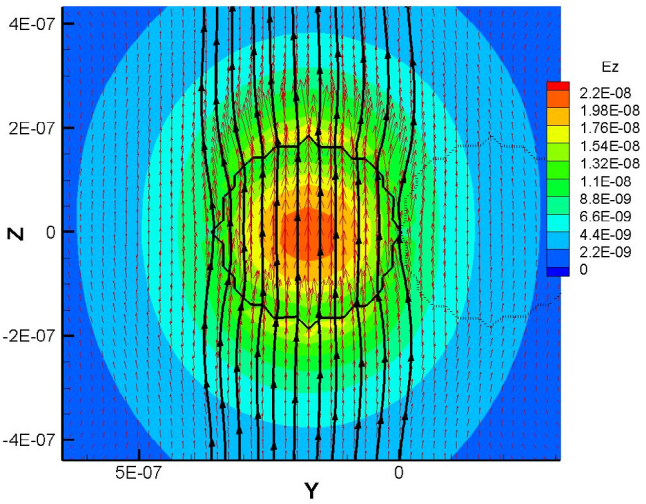

Fig. 7. The predicted contours of E_z at the plane $x = 0$ μm schematic in Fig. 1.

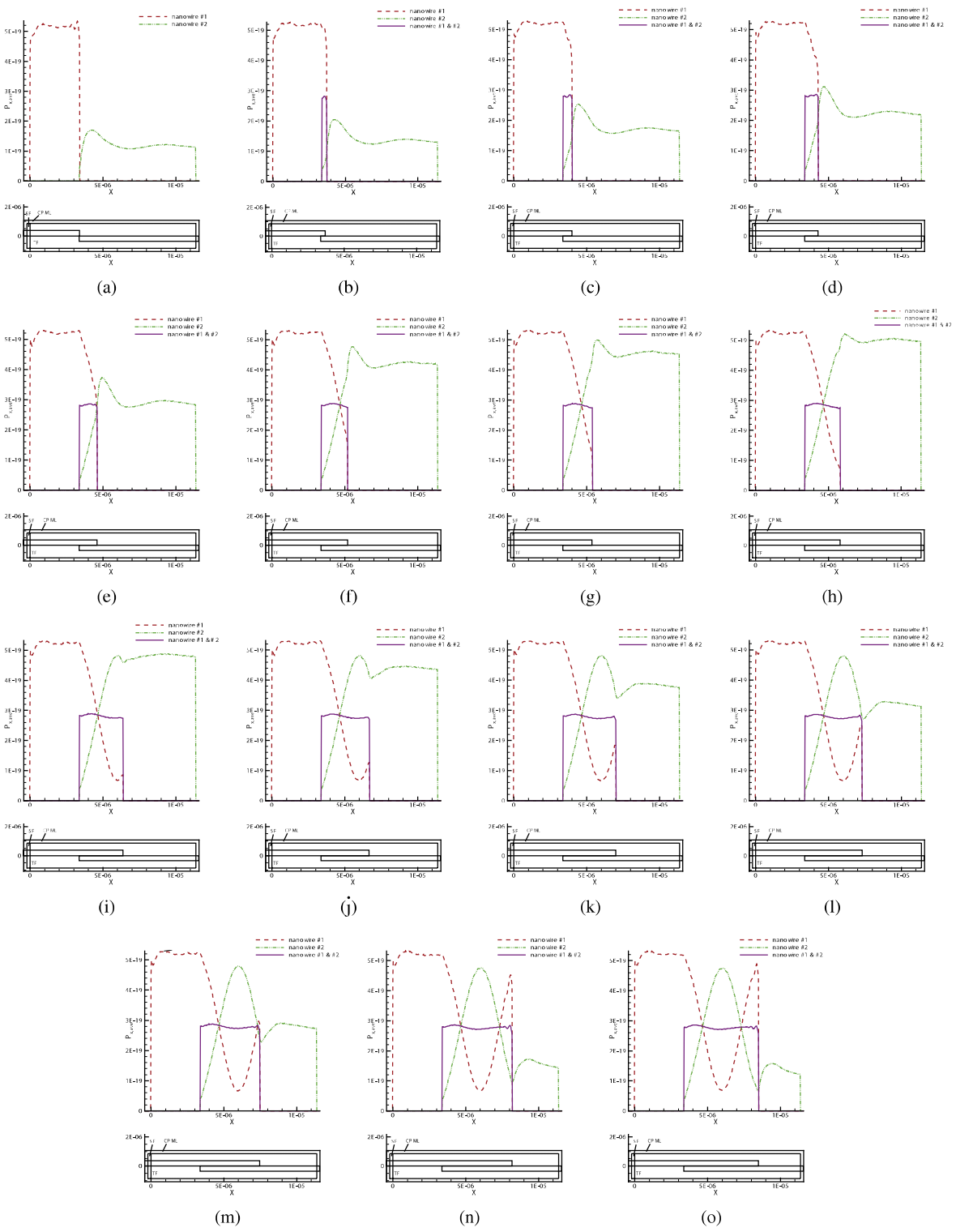

Fig. 8. The predicted averaged values of P_x are plotted with respect to x for the cases investigated at different overlapping lengths. (a) $L = 0.0$ μm; (b) $L = 0.3$ μm; (c) $L = 0.6$ μm; (d) $L = 0.9$ μm; (e) $L = 1.2$ μm; (f) $L = 1.8$ μm; (g) $L = 2.0$ μm; (h) $L = 2.4$ μm; (i) $L = 3.0$ μm; (j) $L = 3.3$ μm; (k) $L = 3.6$ μm; (l) $L = 3.9$ μm; (m) $L = 4.1$ μm; (n) $L = 4.8$ μm; (o) $L = 5.1$ μm.

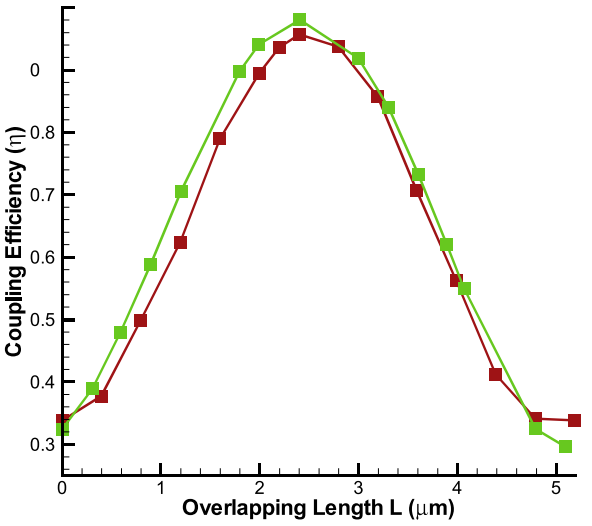

Fig. 9. The predicted evanescent coupling efficiencies are plotted with respect to the chosen overlapping lengths.

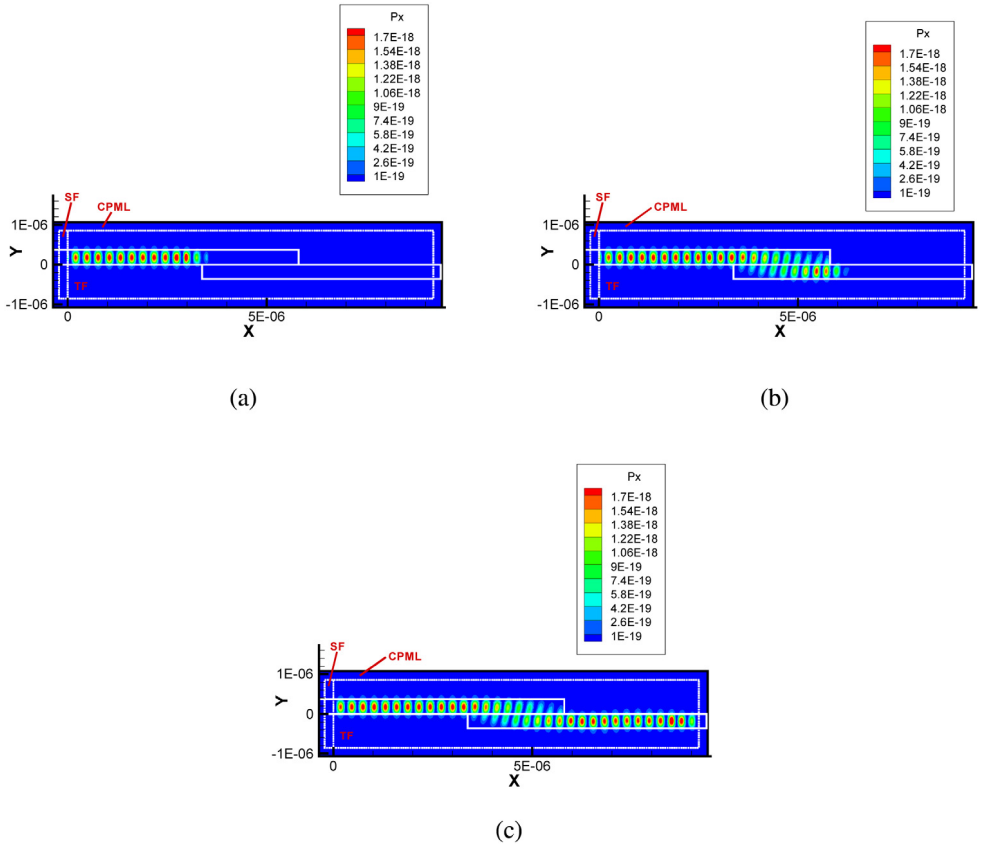

Fig. 10. The predicted contours of P_x ($z = 0$, xy-plane) with respect to time for the case investigated at $L = 2.40625$ μm. (a) $t = 1.98471E - 014$ (s); (b) $t = 3.37108E - 014$ (s); (c) $t = 4.93258$ (s).

is followed by plotting the profiles of the average P_x with respect to x for the cases investigated at different overlapping lengths in Fig. 8. The coupling efficiency is defined below

$$Coupling\ Efficiency \equiv \frac{maximum\ of\ P_{x,ave}(x)\ in\ second\ nanowire\ after\ overlapping\ position}{maximum\ of\ P_{x,ave}(x)\ in\ first\ nanowire\ before\ overlapping\ position}.$$

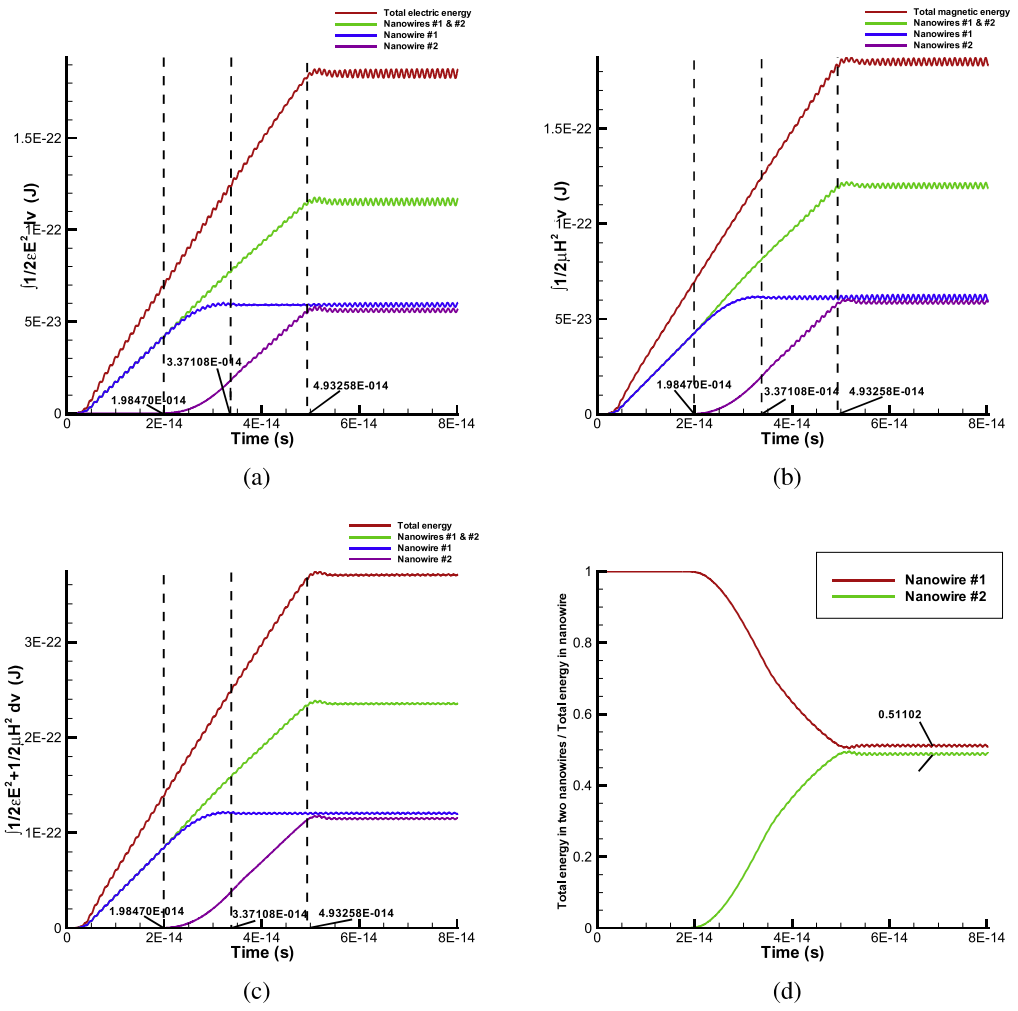

Fig. 11. The electric energies predicted in two nanowires are plotted with respect to time. (a) electric energies; (b) magnetic energies; (c) total energies; (d) ratio of electric and magnetic energies.

Given this definition, we can compute the respective coupling efficiency and plot it with respect to the overlapping length in Fig. 9.

5.2. Electric and magnetic energies in two nanowires

Subjected to a prescribed incident z-dependence wave at the $x = 0$ μm plane, we can compute the time varying values of P_x from the simulated solutions of Maxwell's equations. Take the overlapping length $L = 2.4$ μm as an example, the contours of P_x plotted with respect to time in Fig. 10 show us how the wave energy is propagated from the first nanowire to the second nanowire. Based on the simulated electric and magnetic field solutions, we plot the electric energy $\int \frac{1}{2}\epsilon E^2 dV$ in Fig. 11(a) and the magnetic energy $\int \frac{1}{2}\mu H^2 dV$ in Fig. 11(b) with respect to time. The result of the total energy with respect to time is plotted in Fig. 11(c). Also, the percentages of the total energy in two nanowires are plotted in Fig. 11(d) to indirectly validate the simulated results. We can also compute the time rate of the total energy, or $\frac{\partial}{\partial t}\int(\frac{1}{2}\epsilon E^2 + \frac{1}{2}\mu H^2)dV$, and $\int \underline{P} \cdot d\underline{S}$ and plot them in Fig. 12 within the nanowires.

5.3. Investigation into the EM wave structure in two nanowires

To give a clear structure of the predicted electric and magnetic fields, the predicted contours of $\underline{E}$ and $\underline{H}$ are plotted at some cutting planes. Like the streamlines, which are denoted as a family of curves that are instantaneously tangent to the velocity vector of the fluid flow, in fluid dynamics, we plot the lines of $\frac{d\underline{s}}{|d\underline{s}|} = \frac{\underline{B}}{|\underline{B}|}$ and $\frac{d\underline{s}}{|d\underline{s}|} = \frac{\underline{E}}{|\underline{E}|}$. For the $\underline{B}$ and $\underline{E}$

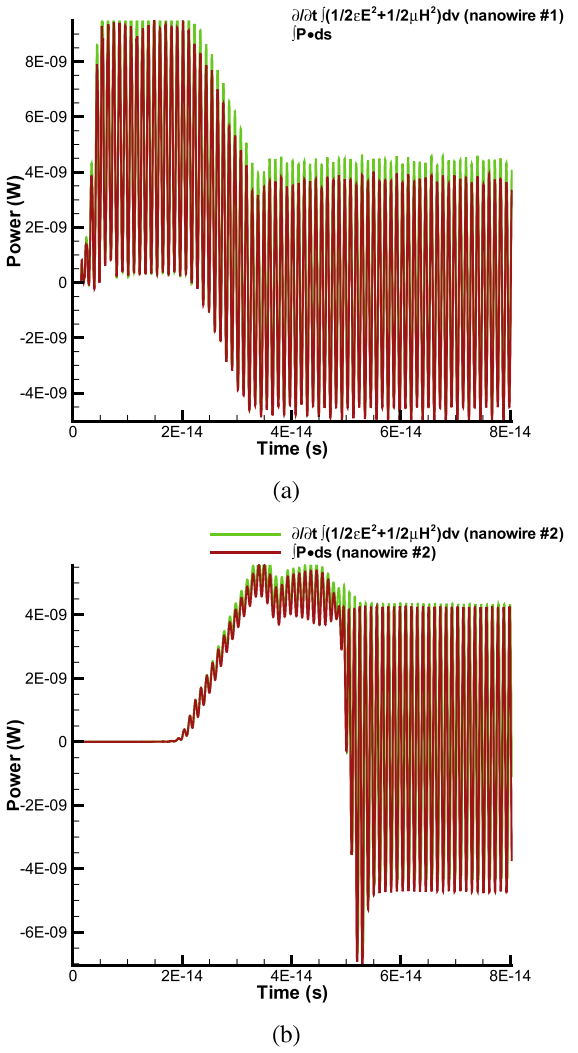

Fig. 12. The predicted values of $\frac{\partial}{\partial t}\int \frac{1}{2}(\epsilon E^2 + \mu H^2)dV$ and $\int \underline{P} \cdot d\underline{S}$ are plotted with respect to time in the (a) first nanowire; (b) second nanowire.

vectors, they are tangent to the magnetic and electric field lines, respectively. The snapshots plotted in Fig. 13 exhibit the magnetic and electric skeletons at $t = 7.29167E - 14$ s. These lines help to reveal the 3D magnetic and electric topologies, respectively. Note that the magnetic and electric field lines are used to depict the electromagnetic vector field. The streaklines, which are the loci of points passing continuously a particular spatial point in the past, are also plotted for the electric and magnetic fields. These plots shed light that information of $\underline{E}$ and $\underline{H}$ injected into the EM field at a fixed point extends along a streakline. One can clearly see from Fig. 14 that the predicted streaklines spiral along the magnetic and electric field lines, respectively.

5.3.1. Three-dimensional skeleton of the electric field

In x-direction, we choose two planes, namely $x = 2.7125E - 06$ m and $x = 2.975E - 06$ m, in the first nanowire and five planes, namely $x = 3.54375E - 06$ m, $x = 3.959375E - 06$ m, $x = 4.571875E - 06$ m, $x = 5.3825E - 06$ m, and $x = 5.665625E - 06$ m in the region of overlapping nanowires, to plot the predicted three-dimensional electric field lines. Our aim is to understand better the coupling effect between the two parallel nanowires.

In Fig. 15(a), the electric field line passing through a point at the $x = 2.7125E - 06$ m plane clearly shows the presence of a spirally configured electric field propagating towards the y-direction in a clockwise (CW) sense. Outside of the first nanowire, the spiralling wave motion of a large radius that is featured with a smaller magnetic field value of $|\underline{E}|$ is seen to propagate towards the core of the first nanowire which is featured with a reduced radius, thereby increasing the electric field strength $|\underline{E}|$. Such a spiralling propagation of the electric field exhibits a wave pattern of increasingly larger spiralled

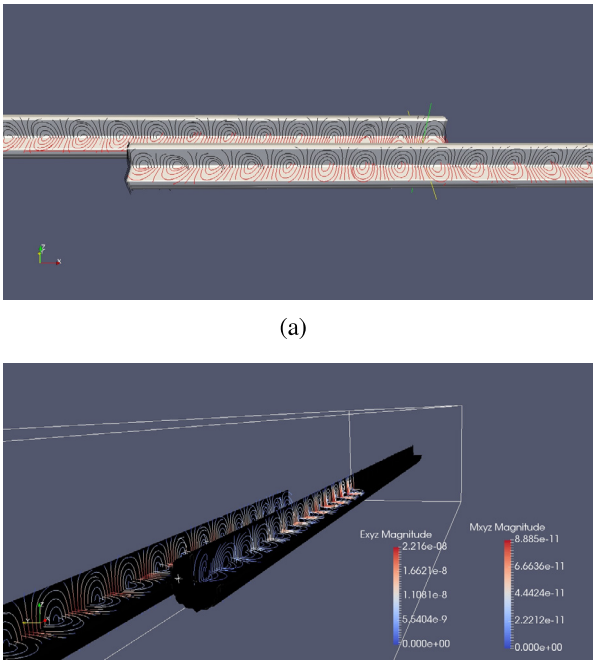

(a)

(b)

Fig. 13. The predicted field lines at $t = 7.29167E - 14$ s. (a) *XY* plane view; (b) *YZ* plane view.

radius and a weaker electric field. The predicted increased magnitudes of $|\underline{E}|$ in the nanowire core and the decreased values of $|\underline{E}|$ at two ends of the field lines confirm the existence of evanescent wave in the presently investigated parallel nanowires. Prior to the second nanowire, the three-dimensional spirallingly configured electric field structure remains the same as that exhibited at the upstream side. The electric field line passing through a point at the plane $x = 3.54375E-06$ m in the overlapping region, the wave skeleton changes sharply in the sense that the electric wave propagates spirally in a counter clockwise (CCW) direction, as shown in Fig. 15(b). The electric wave starting from a point outside of the nanowire propagates into the overlapped nanowires in a clockwise direction (or y-direction) and it then leaves the second nanowire. Afterwards, the phenomenon of wave entry into the overlapped nanowires can be observed in a CCW (or y-direction) fashion. This is followed by an exit from the first nanowire. Similarly, when entering the nanowires, the radius of the spiralling electric wave is decreased with the accompanied enhancement of electric field. The wave structure passing a point at $x = 3.959375E - 06$ m, which is plotted in Fig. 15(c), takes the same form as that shown in Fig. 15(b). At a further downstream plane, the electric field structure at $x = 4.571875E - 06$ m, for example, exhibits a different pattern (Fig. 15(d)). At $x = 5.3825E - 06$ m, the spiralling wave motion proceeds along a CW ($+y$) motion and then a CCW ($-y$) direction in the two overlapped nanowires, as shown in Fig. 15(e). At the plane $x = 5.665625E - 06$ m, the CCW wave pattern remains unchanged. However, from Fig. 15(f) one can see that a CCT (or -y direction) type of wave propagates directly into the second nanowire.

5.3.2. Three-dimensional skeleton of magnetic field

For the sake of completeness, we also plot the three-dimensional magnetic field passing through the points located at three different planes, namely $x = 2.7125E - 06$ m, $x = 2.975E - 06$ m and $x = 2.8E - 06$ m. In Fig. 16(a), one can see a similar magnetic spiralling wave structure as the one described in Section 5.3.1 for the electric field. One can find the wave patterns of decreasing spiralling radius in the wire and an increasing spiralling radius outside the wire (Fig. 16(a)). The field magnitude of $|\underline{B}|$ is larger inside the wire. The difference between the electric and magnetic fields is that the clockwise spiralling motion is directed along the positive z-direction rather than along the y-direction. This is under our expectation because of the fact that the electric and magnetic fields are orthogonal to each other. On the contrary, the 3D magnetic line passing through the point at $x = 2.975E - 06$ m, magnetic wave is propagated in a clockwise sense (or along the $-z$ direction), as shown in Fig. 16(b). The field magnitude $|\underline{B}|$ remains large inside the first nanowire. At a point located closer to the second nanowire, the wave resumes its pattern as shown in Fig. 16(c).

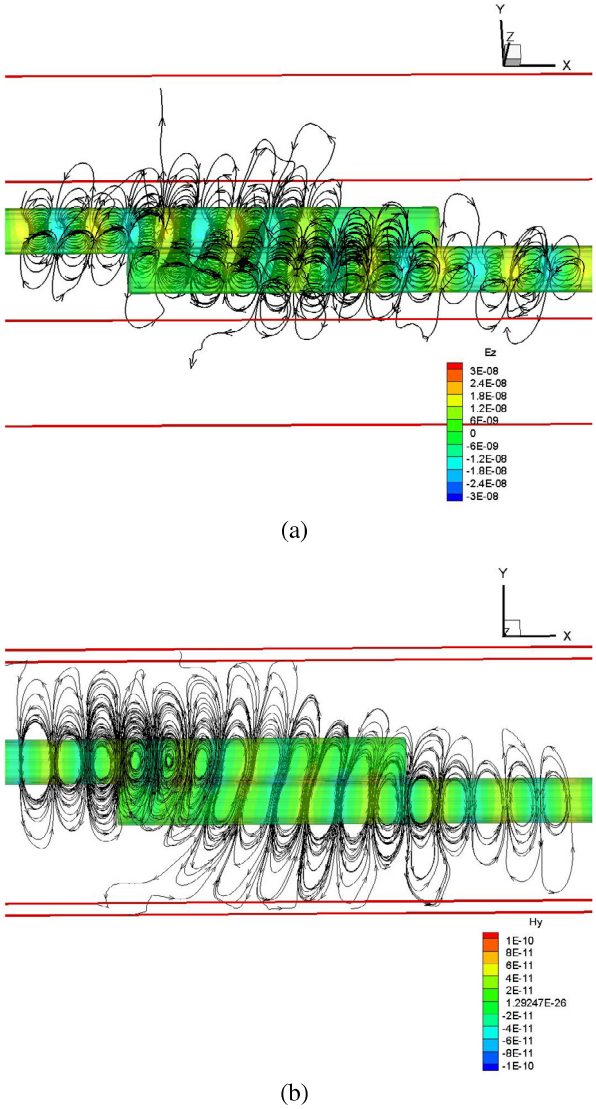

Fig. 14. The predicted streaklines of the electric field at $t = 7.29167E - 14$ s. (a) electric field; (b) magnetic field.

6. Concluding remarks

Three-dimensional Maxwell's equation solver is developed to study the evanescent coupling efficiency of two overlapped parallel silica nanowires. Our aim of the current scheme developments is to numerically preserve symplecticity and conserve Hamiltonians and invariants at all times in the Maxwell's equations. Towards these perspectives, the explicit symplectic partitioned Runge–Kutta time integrator is applied together with the space-centred scheme. For increasing the phase accuracy, the discrepancy between the numerical and exact phase velocities is minimized. The temporally second-order and spatially fourth-order accurate three-dimensional schemes developed on staggered grids for solving the ideal Maxwell's solutions have been numerically verified through one problem with exact solution. The evanescent wave coupling in two nanowires is numerically studied under the fifteen chosen overlapping lengths at the fixed nanowire diameter. Also, the EM wave structures in two wires have been explored and revealed in great detail.

Acknowledgements

This work was supported by the Ministry of Science and Technology (MOST) of the Republic of China under the Grant MOST102-2221-E-002-102-MY3.

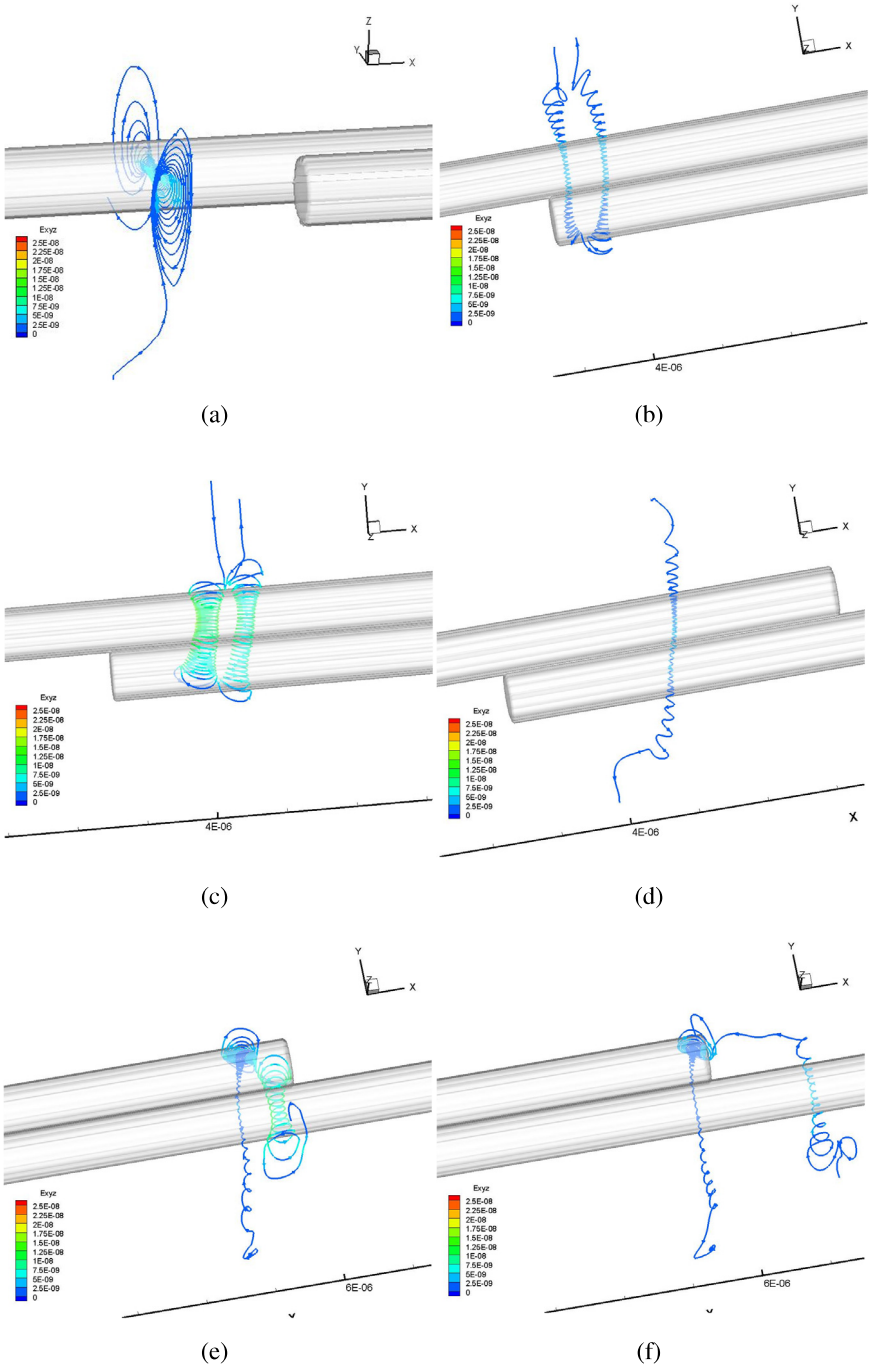

Fig. 15. The predicted streaklines of the electric field passing through some points at $t = 7.29167E - 14$ s. (a) on $x = 2.7125E - 06$ m plane; (b) on $x = 3.54375E - 06$ m plane; (c) on $x = 3.959375E - 06$ m plane (d) on $x = 4.571875E - 06$ m plane (e) on $x = 5.3825E - 06$ m plane (f) on $x = 5.665625E - 06$ m plane.

Funding

This study was funded by MOST102-2221-E-002-102-MY3.

Conflict of interest

The authors declare that there is no conflict of interest.

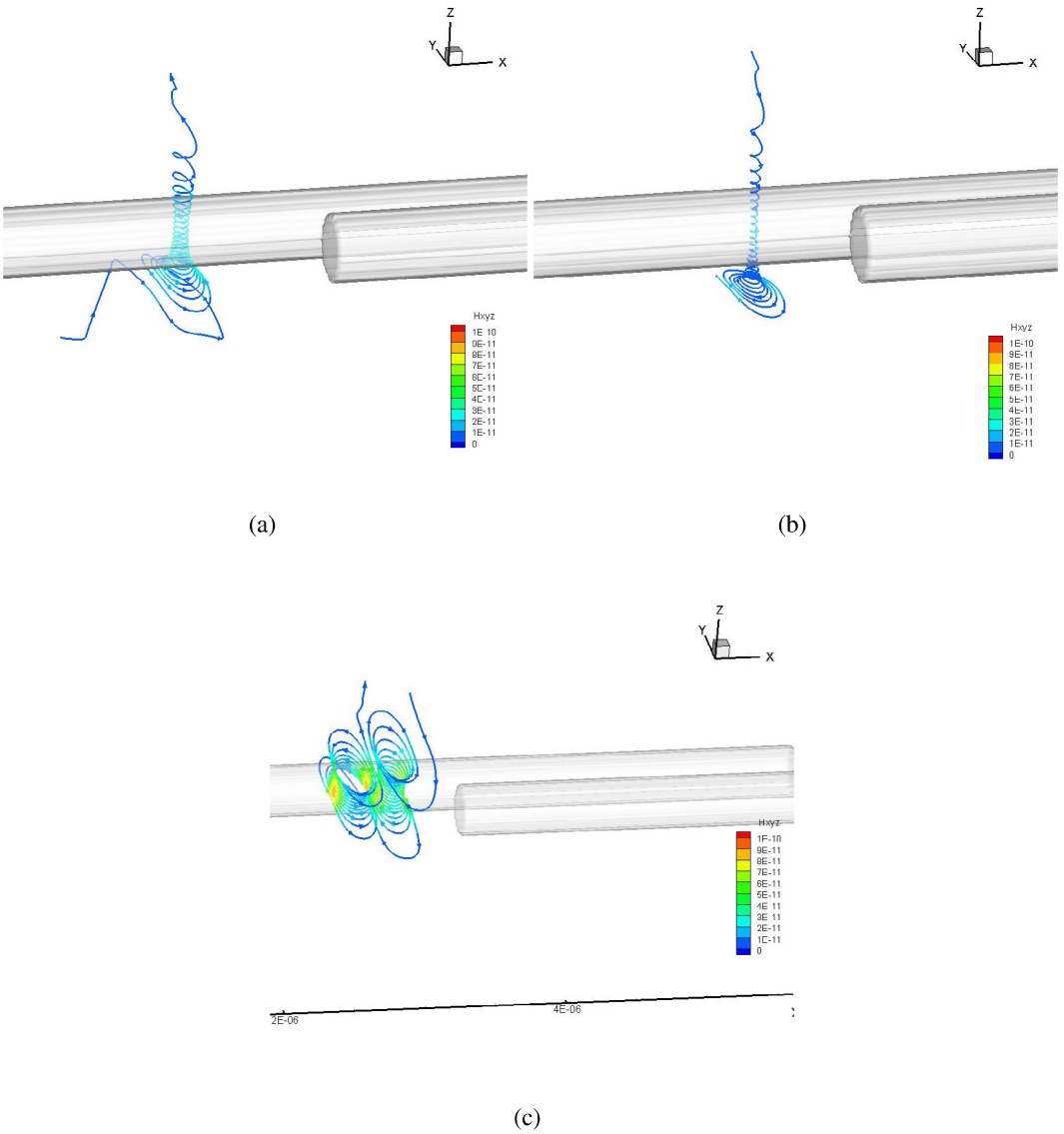

Fig. 16. The predicted streaklines of the magnetic field passing through some selected planes at $t = 7.29167E - 14$ s. (a) on $x = 2.7125E - 06$ m plane; (b) on $x = 2.975E - 06$ m plane; (c) on $x = 2.8E - 06$ m plane.

References

[1] X.Q. Wu, L.M. Tong, Optical microfibers and nanofibers, Nanophotonics 2 (5–6) (2013) 407–428.
[2] K.S. Yee, Numerical solution of initial boundary value problems involving Maxwell's equations in isotropic media, IEEE Trans. Antennas and Propagation 14 (1960) 302–307.
[3] B. Zhu, J. Chen, W. Zhong, Q.H. Liu, A hybrid FETD-FDTD method with nonconforming meshes, Commun. Comput. Phys. 9 (2011) 828–842.
[4] T.T. Zygiridis, T.D. Tsiboukis, Optimized three-dimensional FDTD discretizations of Maxwell's equations on Cartesian grids, J. Comput. Phys. 226 (2007) 2372–2388.
[5] K. Niu, Z. Huang, M, Li, X. Wu, Optimization of the artificially anisotropic parameters in WCS-FDTD method for reducing numerical dispersion, IEEE Trans. Antennas and Propagation 65 (2017) 7389–7394.
[6] N. Anderson, A.M. Arthurs, Helicity and variational principles for Maxwell's equations, Int. J. Electron. 54 (1983) 861–864.
[7] J.E. Marsden, A. Weinstein, The Hamiltonian structure of the Maxwell-Vlasov equations, Physica D 4 (1982) 394–406.
[8] L.D. Landau, E.M. Lifshitz, L.P. Pitaevskii, Electrodynamics of Continuous Media, Pergamon Press, Oxford, 1960.
[9] B. Jiang, J. Wu, L.A. Povinelli, The origin of spurious solutions in computational electromagnetics, J. Comput. Phys. 125 (1996) 104–123.
[10] F. Assous, P. Degond, E. Heintze, P.A. Raviart, J. Serger, On a finite-element method for solving the three-dimensional Maxwell equations, J. Comput. Phys. 109 (1993) 222–237.
[11] L.L. Jiang, J.F. Mao, X.L. Wu, Symplectic finite-difference time-domain method for Maxwell equations, IEEE Trans. Magn. 42 (8) (2006) 1991–1995.

[12] W. Sha, Z.X. Huang, M.S. Chen, X.L. Wu, Survey on symplectic finite-difference time-domain schemes for Maxwell's equations, IEEE Trans. Antennas and Propagation 56 (2008) 493–500.
[13] Z. Huang, J. Xu, B. Sun, X. Wu, A new solution of Schrödinger equation based on symplectic algorithm, Comput. Math. Appl. 69 (2015) 1303–1312.
[14] T.W.H. Sheu, Y.C. Wang, J.H. Li, Development of a 3d staggered FDTD scheme for solving Maxwell's equations in Drude medium, Comput. Math. Appl. 71 (2016) 1198–1226.
[15] J.X. Cai, Y.S. Wang, Y.Z. Gong, Numerical analysis of AVF methods for three-dimensional time-domain Maxwell's equations, J. Sci. Comput. 66 (2016) 141–176.
[16] A.W. Snyder, J.D. Love, Optical Waveguide Theory, Chapman and Hall, New York, NY, 1983.
[17] C.Y. Kao, Investigation Into Nanowire Coupling Efficiency Through the Simulation of Maxwell's Equations (Master thesis), National Taiwan University, 2016.
[18] L.M. Tong, J.Y. Lou, E. Mazur, Single-mode guiding properties of subwavelength-diameter silica and silicon wire waveguides, Opt. Express 12 (2004) 1025–1035.
[19] J.A. Roden, S.D. Gedney, Convolution PML (CPML) : An efficient FDTD implementation of the CFS-PML for arbitrary media, Microw. Opt. Technol. Lett. 27 (2000) 334–339.